International Journal of Heat and Mass Transfer 217 (2023) 124663

Contents lists available at ScienceDirect

International Journal of Heat and Mass Transfer

journal homepage: www.elsevier.com/locate/ijhmt

Three-field mixed *hp*-finite element method for the solution of the Guyer–Krumhansl heat conduction model

Balázs Tóth

Institute of Applied Mechanics, University of Miskolc, Miskolc-Egyetemváros, H-3515, Hungary

ARTICLE INFO

Keywords:
Three-field variational formulation
Weakly-imposed boundary conditions
Mixed FEM
hp-type approximation
Guyer–Krumhansl heat equation
Transient analyzes

ABSTRACT

On the basis of numerous experimental studies the Guyer–Krumhansl heat conductivity model can be considered as one of the most promising theoretical models to simulate the low temperature processes and the thermal behavior of such complex structures as materials with inhomogeneities and interfaces, as well as porous materials. However, the classical *h*-version finite element methods do not provide convergent and accurate results for the solution of the Guyer–Krumhansl heat conductivity model. In recent paper, a new three-field variational formulation is derived treating the temperature, the heat flow and its current density as independent variables. Both the temperature- and the heat flow boundary condition are weakly imposed, i.e., built in the variational form.

Based on this variational background, a new, *hp*-version mixed finite element method is constructed. The *h*- and *p*-convergence behaviors of the temperature and the heat flow are analyzed on the transient region for two representative model problems: (i) a rapid heating process with exponentially changing rate and (ii) a ramp-type heating process. The relative and absolute errors are measured in maximum norm. From the computational experiments it follows that the mixed *hp*-finite element method gives reliable, robust (uniformly stable) results not only for the *h*- but also for the *p*-approximation in the case of both the temperature and the heat flow.

1. Introduction

In the engineering practice the classical Fourier-type heat conductivity equation is applied most often to model the thermal processes. However, in numerous cases, this commercial model does not provide satisfactory results both for modeling heat conduction at room temperatures in heterogeneous materials, being composed by two homogeneous layers (a conductor and an insulator) having different material properties layer-wise, and for describing the thermal processes at low temperature [1–3]. This kind of heterogeneity is included for example in metal and carbon foams, as well as materials with internal cracks and porous materials like soils and rocks. Although in steady state at macro level there is no significant difference between the measured values and the computed results by the Fourier model, these differ from each other in the transient region, yielding a non-Fourier thermal conduction effect, see, for instance, Fig. 1 in [2], as well as these can also differ from each other in steady state transport process at nano level, see [4].

Accordingly, from the experiments it follows that the basic theory, i.e., the Fourier model has to be modified. The results provided by the Guyer–Krumhansl heat conductivity equation [5] as one of the non-Fourier heat conductivity equations shows a very good agreement with the measurement data. Besides, the two-temperature thermodynamic models also give physically well-justified alternatives for modeling thermal processes in heterogeneous materials at room temperature, see [6–8]. In the case of the two-temperature models, the appropriate treatment of the boundary conditions (mainly the heat flow boundary condition) and the coupling play an important role especially for inhomogeneous materials, however, the applied numerical scheme is less essential or it has no significant influence on the accuracy and stability of the solution. From physical point of view these models are more interesting while from numerical/finite element (FE) and mathematical/variational point of view the solution of the Guyer–Krumhansl model is more challenging task even in 1D case.

In recent paper, as a first step, we choose the Guyer–Krumhansl heat conductivity model, following the experimental results and measurement data in [1,2]. This constitutive model contains the material parameter κ^2 and the relaxation time τ as two new material constants. The relaxation time is usually much smaller than about 10^{-5} s for metals and liquids [9,10]. However, some experimental studies exhibit that the value of τ can be higher for glass, sand [11] and organic materials,

E-mail address: mechtb@uni-miskolc.hu.

https://doi.org/10.1016/j.ijheatmasstransfer.2023.124663
Received 21 July 2023; Received in revised form 20 August 2023; Accepted 30 August 2023
Available online 15 September 2023

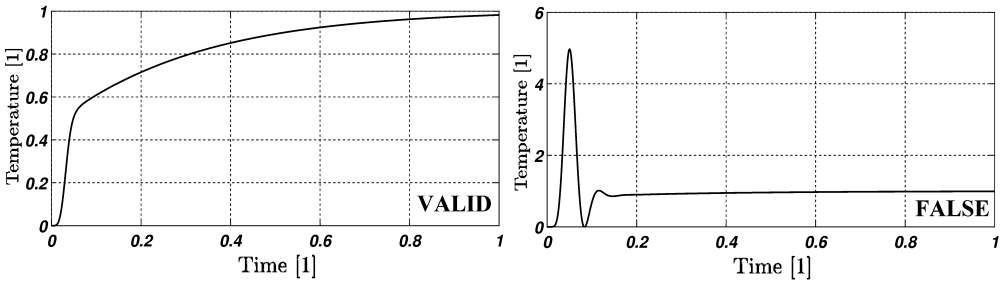

Fig. 1. Illustrative solutions for the Guyer–Krumhansl model for the same parameter setting [20]. Left: the analytic solution is plotted for the dimensionless temperature series. Right: COMSOL's solution.

tissues [9,10], as well as processed meat [12]. The material constant κ^2 is associated with the mean free path arising from the kinetic theory or the non-equilibrium thermodynamics with internal variables, see [13,14].

In the case of the Guyer–Krumhansl heat conductivity model the heat flow boundary condition (BC) can not be treated as Neumann-type BC prescribed on temperature derivative because in this case the heat flow can not be determined directly from the temperature gradient. The partial differential equation system becomes more complex, i.e., the solution of the Guyer–Krumhansl heat conductivity model directly either for the temperature or for the heat flow is a very difficult, challenging task, considering either the temperature or the heat flow as basic or primary variable. Analytically, it is possible only for some specific BCs by the aid of the methodology of separation of variables, using the Fourier series expansion- and the operational approaches for the solution of the Guyer–Krumhansl model, see the works [15–17] and [18,19].

The FE model of any types of partial differential equations can be implemented within the framework of the software COMSOL Multiphysics. Thus, for example, in [20] the Guyer–Krumhansl model was tried to be solved numerically using COMSOL's Mathematics Module in version v5.3a which unfortunately is not able to reproduce the temperature response curves at all, giving a very bad results with large oscillations and high error values. Also, similarly wrong situations can be experienced for the FE solution of the ballistic-conductive equation [20]. Namely, the FE solution computed by COMSOL does not show a good agreement with the analytic (reference) solution even for very fine mesh.

In details three typical settings were analyzed: $\kappa^2 = 0$ leading to the Maxwell–Cattaneo–Vernotte equation, $\kappa^2/\tau = \alpha$ reproducing Fourier's solution, and $\kappa^2/\tau > \alpha$ producing over-diffusive solutions, with $\alpha = \lambda/(\rho c_V)$ being the thermal diffusivity. In the first two situations, COMSOL can provide a physically valid temperature series, although its resource requirements – CPU and RAM usage – are very high. However, in the last one in which $\kappa^2/\tau > \alpha$, the response temperature series was found to be far from realistic [20], absolutely wrong solutions can easily be obtained for a stable and seemingly convergent method. These solutions do not depend on the applied mesh and time-stepping algorithm. Fig. 1 compares the physically valid temperature and the wrong one obtained from COMSOL, demonstrating the importance and the necessity of a robust FEM.

In the last years, the development of reliable and efficient numerical methods for the solution of the Guyer–Krumhansl heat equation was motivated by the above-mentioned drawback. So far, the current results achieved have not been so satisfactory yet. More recent, this is the reason why an increasing interest can be experienced in this research direction. An alternative way, to overcome the numerical difficulties aforementioned, is to construct an advanced finite difference method, for example, the shifted fields scheme as space discretization technique called symplectic algorithms [20,21]. In this case, the heat flow and the temperature are treated as independent variables and the locations of the temperature values are shifted by a half space step size with respect to the locations of the heat flow values, thereby allowing the direct prescription of the heat flow BC if necessary.

Another alternative to avoid the numerical difficulties is to construct *hp*-version mixed FEM. Namely, most of the FE softwares and packages use (i) the lowest-order polynomial, i.e., linear approximations for the unknown basic variable and (ii) usually solve the resulting system for one (primary) variable, as well as (iii) apply the Fourier-type heat conductivity model to predict the thermal processes [22–24]. Furthermore, the required accuracy is reached with mesh refinement, using the lowest-order polynomial approximation for each FE. In some papers [25–31] classical *h*-version FEMs were elaborated on the Maxwell–Cattaneo–Vernotte-version of the heat conductivity model (when the parameter κ^2 is equal to zero), or the dual-phase-lag equations, see their exact and approximate theories, for example, in [32]. Nevertheless, now, from practical point of view, these latter theoretical models are less interesting for the considered model problems.

As seen, for example, in [20], the standard, mesh refinement-based FEMs can produce low convergence rates and large inaccuracy, or in even worse cases, oscillatory behavior equipped with high amplitude and frequency for certain kinds of initial-boundary value problems (IBVP) and when some of the material constants or the characteristic size of the body approach their limit value [33]. In order to circumvent these numerical phenomena, the *p*-type extension will be employed as a hierarchic higher-order approximation technique having outstanding computational performance. This was originally devised for one-field variational formulations in [34,35], then further-developed for the stress-, deformation- and natural frequency analysis of shells of revolution, as well as heat equation, based on hybrid/mixed and ultra-weak variational approaches (discontinuous Petrov–Galerkin technology) in [36–40].

For smooth problem the *p*-version FEMs based on one-field primal variational formulations exhibit exponential convergence being featured by a curve equipped with increasing negative slope while the asymptotic convergence rate of the uniform *h*-refinement is of algebraic type which can be represented by a straight line, i.e., the rate of *p*-convergence is much faster than that of the *h*-convergence [35,41,42]. Upon the combination of a properly chosen (graded) mesh refinement strategy with a simultaneous increasing polynomial degree (*hp*-technology) we will have again an exponential convergence in energy norm computations even for non-smooth problems as well [35,41,42]. These promising properties motivate our research work.

In accordance with the numerical difficulties and their possible solutions, mentioned above, the aim of this paper is to present a new mixed *hp*-version FEM based on a three-field variational formulation for reliable and efficient solution of the Guyer–Krumhansl heat conductivity model in the refined theories of thermodynamics.

The paper is organized as follows. After having collected the partial differential equations, as well as the BCs and the initial conditions (IC), i.e., the second-order differential equation system of the Guyer–Krumhansl heat conductivity model, the current density of heat flow is systematically introduced as intermediate variable beside the temperature and the heat flow, resulting in a first-order differential equation system, then a new three-field variational formulation is derived keystepwise in Section 2. Based on this variational background a new

mixed *hp*-version FEM method is presented in Section 3. In Section 4 the computational performance of the mixed *hp*-FEM is tested through a comprehensive *h*- and *p*-convergence analysis on the two following representative benchmark problems: (i) a rapid heating process with exponentially changing rate and (ii) a ramp-type heating process. The paper is closed by the concluding remarks and an outline of the future research work.

2. Mathematical model

In this section a new three-field mixed variational formulation will be derived for the solution of the Guyer–Krumhansl model as one of the refined thermodynamic models. This will serve as a mathematical basis for the related higher-order FEM suitable for the accurate numerical solution of the considered heat conductivity model.

2.1. Governing equations

In this subsection the basic differential equations of the Guyer–Krumhansl model are collected and the corresponding BCs and ICs are listed in details. Let us consider now a rigid body occupying the space domain $\overline{\Omega} = [0, \ell]$ at a certain time instant $t \in \overline{I}$, where ℓ denotes the length of the body (domain) and $\overline{I} = [t_0, t_1]$ defines a closed temporal domain, here t_0 and t_1 are two given time instants for which $t_1 > t_0$. In the model problem we suppose that the body is subjected to the internal heat resource $r(t,x)$ in $\overline{I} \times \Omega$ and the prescribed external heat flow $\tilde{q}(t)$ at $x = \ell$, while the temperature $\tilde{T}(t)$ is specified in time at $x = 0$ for the sake of generality. The governing differential equations modeling the thermal conductivity process are given along with the BCs and the ICs in the following:

Energy equation

$$\rho c_V \dot{T} + q' = r \quad \text{in } (t_0, t_1] \times \Omega\,, \tag{1}$$

as entropy balance law, where ρ and c_V are the material density and the specific heat at constant volume, as well as the prime (or double prime) in the superscript means first (or second) partial derivative with respect to the space coordinate x and the dot over a variable indicates partial time derivative,

Constitutive equation

$$\tau \dot{q} + q + \lambda T' - \kappa^2 q'' = 0 \quad \text{in } (t_0, t_1] \times \Omega \tag{2}$$

as heat conductivity law, in which τ, λ and κ^2 are the relaxation time, the heat conductivity coefficient and the "newly-introduced" heat parameter as material constants, for the sake of generality, the body is subjected to the following

Spatial prescriptions

$$T(t,0) = \tilde{T}(t) \quad \text{in } \overline{I}\,, \tag{3}$$

$$q(t,\ell) = \tilde{q}(t) \quad \text{in } \overline{I}\,, \tag{4}$$

as BCs on the temperature and heat flow at $x = 0$ and $x = \ell$, respectively, as well as

Temporal prescriptions

$$T(t_0,x) = T_0(x) \quad \text{and} \quad q(t_0,x) = q_0(x) \quad \text{in } \overline{\Omega} \tag{5}$$

as ICs at the time instant $t_0 = 0$ s, keeping in mind the compatibility criteria $\tilde{T}(0) = T_0(0)$ and $\tilde{q}(t_0) = q_0(\ell)$ on the prescribed quantities.

In order to avoid the appearance of the second spatial derivative, i.e., decrease the differential order of the system, let us introduce now the current density of the heat flux, $Q(t,x)$, as intermediate variable in the following way: let $Q = q'$, in this case the two-variable, second-order differential equation system (1)–(2) is transformed into the three-field, first-order form

$$\rho c_V \dot{T} + q' = r \quad \text{in } (t_0, t_1] \times \Omega\,, \tag{6}$$

$$\tau \dot{q} + q + \lambda T' - \kappa^2 Q' = 0 \quad \text{in } (t_0, t_1] \times \Omega\,, \tag{7}$$

$$Q - q' = 0 \quad \text{in } (t_0, t_1] \times \Omega\,. \tag{8}$$

It is worth noting here that this system exhibits a very similar structure to the equations of the ballistic-conductive heat conductivity model. In what follow, the three-field system (6)–(8) together with the BCs (3)–(4) and the ICs (5) as strong form will be reformulated in a weak sense.

2.2. Three-field variational formulation

In this subsection a three-field variational formulation will be derived for the solution of the Guyer–Krumhansl heat conductivity model within the refined thermodynamic concept. Similarly to the systematic procedures presented in [43,44] but without time integration; as the first step in the derivation, the energy equation is weakened, i.e., we multiply Eq. (6) with the test function u, then the obtained expression is integrated over the domain Ω. This procedure yields the variational equation

$$\int_\Omega \left(\rho c_V \dot{T} + q' - r\right) u \,\mathrm{d}\Omega = 0 \tag{9}$$

which can be considered as the weakened version of the energy equation (6). In the second step of the derivation the intermediate equation (8) is relaxed. Accordingly, multiplying Eq. (8) with the test function w, then integrating the obtained result over the domain Ω, we have

$$\int_\Omega \left(Q - q'\right) w \,\mathrm{d}\Omega = 0\,. \tag{10}$$

Then using the partial integration rule

$$\int_\Omega q' \, w \,\mathrm{d}\Omega = [q\, w]_0^\ell - \int_\Omega q \, w' \,\mathrm{d}\Omega \tag{11}$$

and building-in the heat flow BC (4) at $x = \ell$, the second term of Eq. (10) becomes

$$\int_\Omega q' \, w \,\mathrm{d}\Omega = \tilde{q}(t)\, w(\ell) - q(t,0)\, w(0) - \int_\Omega q \, w' \,\mathrm{d}\Omega\,, \tag{12}$$

the substitution of which into Eq. (10) results in the variational integral

$$\int_\Omega Q \, w \,\mathrm{d}\Omega + \int_\Omega q \, w' \,\mathrm{d}\Omega = \tilde{q}\, w(\ell) - q(t,0)\, w(0) \tag{13}$$

that is the relaxed version of the intermediate equation (10). As the third step of the derivation, the constitutive equation is semi-relaxed. Firstly, multiplying Eq. (7) with the test function v and integrating it over the region Ω, we obtain its weak form

$$\int_\Omega \left(\tau \dot{q} + q + \lambda T' - \kappa^2 Q'\right) v \,\mathrm{d}\Omega = 0\,, \tag{14}$$

to only the third term of which, then applying again the partial integration rule

$$\int_\Omega T' \, v \,\mathrm{d}\Omega = [T\, v]_0^\ell - \int_\Omega T \, v' \,\mathrm{d}\Omega \tag{15}$$

and building-in the temperature BC (3) at $x = 0$ we arrive at the integral expression

$$\int_\Omega T' \, v \,\mathrm{d}\Omega = T(t,\ell)\, v(\ell) - \tilde{T}(t)\, v(0) - \int_\Omega T \, v' \,\mathrm{d}\Omega \tag{16}$$

Upon substitution of the latter equation into Eq. (14) we have the semi-relaxed version of the constitutive equation

$$\int_\Omega \tau\,\dot{q}\,v\,\mathrm{d}\Omega + \int_\Omega q\,v\,\mathrm{d}\Omega - \int_\Omega \lambda\,T\,v'\,\mathrm{d}\Omega - \int_\Omega \kappa^2\,Q'\,v\,\mathrm{d}\Omega = \lambda\,\tilde{T}\,v(0) - \lambda\,T(t,\ell)\,v(\ell) \tag{17}$$

Collecting now all of the obtained variational equations, i.e., Eqs. (9), (13) and (17), a new, three-field variational formulation can be stated as theoretical basis necessary for the construction of the higher-order FEM. Accordingly, in this variational problem we seek the triplet $T \in L^2(\Omega)$, $(q, Q) \in H^1(\Omega)$ as trial functions, satisfying *a priori* the temporal prescriptions (5) on the temperature T and the heat flow q, in such a way that the variational integrals

$$\int_\Omega \rho\,c_V\,\dot{T}\,u\,\mathrm{d}\Omega + \int_\Omega q'\,u\,\mathrm{d}\Omega = \int_\Omega r\,u\,\mathrm{d}\Omega \quad \forall u \in L^2(\Omega)\,, \tag{18}$$

$$-\int_\Omega \tau\,\dot{q}\,v\,\mathrm{d}\Omega - \int_\Omega q\,v\,\mathrm{d}\Omega + \int_\Omega \lambda\,T\,v'\,\mathrm{d}\Omega + \int_\Omega \kappa^2\,Q'\,v\,\mathrm{d}\Omega = \lambda\,T(t,\ell)\,v(\ell) - \lambda\,\tilde{T}\,v(0) \quad \forall v \in H^1(\Omega)\,, \tag{19}$$

$$\int_\Omega Q\,w\,\mathrm{d}\Omega + \int_\Omega q\,w'\,\mathrm{d}\Omega = \tilde{q}\,w(\ell) - q(t,0)\,w(0) \quad \forall w \in H^1(\Omega) \tag{20}$$

hold true for all test functions defined on the above-given function spaces. Here, $H^1(\Omega)$ indicates the first-order Sobolev function space interpreted on Ω [45], demonstrating the regularity property for the variable pairs (q, Q) and (v, w), whereas $L^2(\Omega)$ denotes square integrable function space for the variables T and u. Neglecting now the heat source term r, as well as dividing Eq. (19) by λ after having considered that $\lambda > 0$, the variational equations (18)–(20) can be written in the form

$$\rho\,c_V \int_\Omega \dot{T}\,u\,\mathrm{d}\Omega + \int_\Omega q'\,u\,\mathrm{d}\Omega = 0 \quad \forall u \in L^2(\Omega)\,, \tag{21}$$

$$-\frac{\tau}{\lambda}\int_\Omega \dot{q}\,v\,\mathrm{d}\Omega - \frac{1}{\lambda}\int_\Omega q\,v\,\mathrm{d}\Omega + \int_\Omega T\,v'\,\mathrm{d}\Omega + \frac{\kappa^2}{\lambda}\int_\Omega Q'\,v\,\mathrm{d}\Omega = T(t,\ell)\,v(\ell) - \tilde{T}\,v(0) \quad \forall v \in H^1(\Omega)\,, \tag{22}$$

$$\int_\Omega Q\,w\,\mathrm{d}\Omega + \int_\Omega q\,w'\,\mathrm{d}\Omega = \tilde{q}\,w(\ell) - q(t,0)\,w(0) \quad \forall w \in H^1(\Omega) \tag{23}$$

for homogeneous materials. It is important to highlight here that the two main advantageous properties are the following: (i) the three-field variational principle consists of only first-order spatial derivative and (ii) both the temperature and the heat flow BC are ensured in weak form, i.e., built in the variational formulation, these are not handled as subsidiary conditions to the variational form.

3. *hp*-version mixed finite element method

In this section a new, stable *hp*-type mixed FEM will be presented for the solution of the Guyer–Krumhansl thermodynamic model which is based on the three-field variational formulation detailed in the latter section. In what follows, for the sake of simplicity our investigations will be restricted to (piece-wise) homogeneous materials, which now are not subjected to the internal heat source. Therefore, the *hp*-FE discretization of the newly-derived three-field variational integrals (21)–(23) will be presented in the following.

Let us consider now the partitioning the physical domain Ω. Thus, Ω is divided into n sub-domain. Henceforward, the standard element $\Omega_{\mathrm{st}} := \{\xi \mid -1 < \xi < 1\}$ is mapped onto the e-th physical element $\Omega_{\mathrm{el}}^e := \{x \mid x_e < x^e < x_{e+1}\}$ with the node numbers e and $e+1$ by the transformation $x^e := N_1(\xi)x_e + N_2(\xi)x_{e+1}$ alongside the Jacobian $J^e = \ell^e/2$, where $N_1 = (1-\xi)/2$ and $N_2 = (1+\xi)/2$ are the external shape functions while ℓ^e is the length of e-th element and x_e and x_{e+1} are its nodal coordinates ($e = 1, \dots, n$). Accordingly, now the geometric mapping is linear between the standard and the physical elements.

Table 1
Degrees of the applied polynomial approximation spaces.

Trial functions			Test functions		
T	q	Q	u	v	w
p	$p+1$	$p+1$	p	$p+1$	$p+1$

Taking into account the space regularity properties of the trial functions T, q and Q, as well as the test functions u, v and w, i.e., for which using symmetric functional settings those are approximated on each element as

$$T^e(t,\xi) = \sum_{i=1}^{p} T_i^e(t)N_i(\xi)\,, \qquad u^e(\xi) = \sum_{i=1}^{p} u_i^e\,N_i(\xi)\,, \tag{24}$$

$$q^e(t,\xi) = \sum_{i=1}^{p+1} q_i^e(t)N_i(\xi)\,, \qquad v^e(\xi) = \sum_{i=1}^{p+1} v_i^e\,N_i(\xi)\,, \tag{25}$$

$$Q^e(t,\xi) = \sum_{i=1}^{p+1} Q_i^e(t)N_i(\xi) \qquad w^e(\xi) = \sum_{i=1}^{p+1} w_i^e\,N_i(\xi)\,, \tag{26}$$

where $T_i^e(t)$, $q_i^e(t)$ and $Q_i^e(t)$, as well as u_i^e, v_i^e and w_i^e are the unknown time-dependent-, as well as time-independent coefficients, respectively. The mixed *hp*-FE polynomial function space is up-built by the previously-defined external shape functions N_1 and N_2 for the linear approximations ($p = 1$), as well as the internal shape functions $N_j(\xi) = [P_{j-1}(\xi) - P_{j-3}(\xi)]/\sqrt{2(2j-3)}$ called "bubble modes" as integrated Legendre polynomials for the higher-order approximations ($p \geq 2$), where $P_j(\xi)$ are the orthogonal Legendre polynomials, $k = 3, 4, \dots, p+1$ [35,41,42]. The degrees of the applied polynomial approximation space are collected for the independent trial- and test functions in Table 1 as well. Here p is the actual polynomial degree on each element.

Let us write down now the variational integrals (21)–(23) in matrix notations in terms of the coefficients of the temperature, the heat flow and the current density of heat flow. For the sake of simplicity let ${}^{\mathrm{hp}}\boldsymbol{t}$ and ${}^{\mathrm{hp}}\boldsymbol{q}$, as well as ${}^{\mathrm{hp}}\boldsymbol{Q}$ denote the column vectors associated with the time-dependent unknown coefficients of the temperature and the heat flow, as well as the coefficients of the current density of heat flow, respectively. After having carried out the numerical integrations on each element e and taking the regularity properties of the trial and test function into consideration, the *hp*-FE assembling procedure leads to the following time-dependent matrix algebraic equation system

$$\begin{aligned} \mathcal{C}\,{}^{\mathrm{hp}}\dot{\boldsymbol{t}} + \mathcal{K}^T\,{}^{\mathrm{hp}}\boldsymbol{q} &= \boldsymbol{0}\,,\\ -\mathcal{T}\,{}^{\mathrm{hp}}\dot{\boldsymbol{q}} - \mathcal{S}\,{}^{\mathrm{hp}}\boldsymbol{q} + \mathcal{K}\,{}^{\mathrm{hp}}\boldsymbol{t} + \kappa^2/\lambda\,\mathcal{R}^T\,{}^{\mathrm{hp}}\boldsymbol{Q} &= \boldsymbol{g}\,,\\ \mathcal{W}\,{}^{\mathrm{hp}}\boldsymbol{Q} + \mathcal{R}\,{}^{\mathrm{hp}}\boldsymbol{q} &= \boldsymbol{h}\,. \end{aligned} \tag{27}$$

Since the last equation of this system does not depend on the partial time derivative of the unknown functions at all, at each time step ${}^{\mathrm{hp}}\boldsymbol{Q}$ can be expressed directly in terms of ${}^{\mathrm{hp}}\boldsymbol{q}$ as

$${}^{\mathrm{hp}}\boldsymbol{Q} = -\mathcal{W}^{-1}\,\mathcal{R}\,{}^{\mathrm{hp}}\boldsymbol{q} + \mathcal{W}^{-1}\,\boldsymbol{h}\,, \tag{28}$$

upon substitution of which for ${}^{\mathrm{hp}}\boldsymbol{Q}$ into the second equation of the system (27) we have

$$\begin{aligned} \mathcal{C}\,{}^{\mathrm{hp}}\dot{\boldsymbol{t}} + \mathcal{K}^T\,{}^{\mathrm{hp}}\boldsymbol{q} &= \boldsymbol{0}\,,\\ -\mathcal{T}\,{}^{\mathrm{hp}}\dot{\boldsymbol{q}} + \mathcal{K}\,{}^{\mathrm{hp}}\boldsymbol{t} + \tilde{\mathcal{W}}\,{}^{\mathrm{hp}}\boldsymbol{q} &= \tilde{\boldsymbol{g}}\,, \end{aligned} \tag{29}$$

that can be simplified into the form

$$\mathcal{A}\,{}^{\mathrm{hp}}\dot{\boldsymbol{\alpha}} + \mathcal{B}\,{}^{\mathrm{hp}}\boldsymbol{\alpha} = \boldsymbol{f}\,, \tag{30}$$

where

$${}^{\mathrm{hp}}\boldsymbol{\alpha} = \begin{bmatrix} {}^{\mathrm{hp}}\boldsymbol{t} \\ {}^{\mathrm{hp}}\boldsymbol{q} \end{bmatrix}, \quad \mathcal{A} = \begin{bmatrix} \mathcal{C} & \boldsymbol{0} \\ \boldsymbol{0} & -\mathcal{T} \end{bmatrix}, \quad \mathcal{B} = \begin{bmatrix} \boldsymbol{0} & \mathcal{K}^T \\ \mathcal{K} & \tilde{\mathcal{W}} \end{bmatrix} \quad \text{and} \quad \boldsymbol{f} = \begin{bmatrix} \boldsymbol{0} \\ \tilde{\boldsymbol{g}} \end{bmatrix}, \tag{31}$$

in which

$$\tilde{\mathcal{W}} = -\mathcal{S} - \kappa^2/\lambda\, \mathcal{R}^T\, \mathcal{W}^{-1}\, \mathcal{R} \qquad \text{and} \qquad \tilde{\boldsymbol{g}} = \boldsymbol{g} - \kappa^2/\lambda\, \mathcal{R}^T\, \mathcal{W}^{-1}\, \boldsymbol{h}\,, \tag{32}$$

whereas $\mathcal{C}$ and $\mathcal{T}$, as well as $\mathcal{S}$ and $\mathcal{W}$ stand for the consistent matrices of the specific heat and the relaxation, as well as the other heat conductivity parts, respectively, while $\mathcal{K}$ and $\mathcal{R}$ denote the consistent coupling matrices of the system and the column vectors $\boldsymbol{g}$ and $\boldsymbol{h}$ are responsible for the weak satisfaction of the BCs.

4. Computational examples

In this section, the numerical ability of newly-constructed three-field mixed *hp*-FEM will be investigated for two IBVPs as benchmarks problems: the body will be exposed to (i) a heat flow changing with a high, exponential rate and (ii) a ramp-type temperature jump at the left hand side ($x = 0$), concentrating on the transient behavior of the FE solution in both model problems.

4.1. Error measures and parameter settings

The *h*- and *p*-convergences of the relative and absolute error will be measured point-wise in the maximum norm of the time series of temperature and heat flow

$$\hat{e}^{\mathrm{hp}} = \frac{\max\limits_{t\in[t_0,t_1]} \left| {}^{\mathrm{hp}}\boldsymbol{t} - \boldsymbol{t}_{\mathrm{ref}} \right|}{\max\limits_{t\in[t_0,t_1]} \left| \boldsymbol{t}_{\mathrm{ref}} \right|} \quad \text{and} \quad \hat{e}^{\mathrm{hp}} = \frac{\max\limits_{t\in[t_0,t_1]} \left| {}^{\mathrm{hp}}\boldsymbol{q} - \boldsymbol{q}_{\mathrm{ref}} \right|}{\max\limits_{t\in[t_0,t_1]} \left| \boldsymbol{q}_{\mathrm{ref}} \right|}\,,$$

$$\text{as well as} \quad e^{\mathrm{hp}} = \max_{t\in[t_0,t_1]} \left| {}^{\mathrm{hp}}\boldsymbol{q} - \boldsymbol{q}_{\mathrm{ref}} \right| \tag{33}$$

at both the left-hand-sided- and the right-hand-sided boundary, $x = 0$ and $x = \ell$, where $\boldsymbol{t}_{\mathrm{ref}}$ and $\boldsymbol{q}_{\mathrm{ref}}$ are the reference solutions for the temperature and heat flow computed by the use of a very fine uniform FE mesh along with high-degree approximation on each element ($n = 100$ and $p = 11$). The reference solutions are also validated by the exact solution for which the details can be found in [2,15,16] and in [33,46] with neglecting the linear elastic effects. During the convergence test, the number of degrees of freedom (DOF) is equal to the size of the vector $\boldsymbol{\alpha}$ consisting of the unknown coefficients of the system (30).

The observed bodies with length $\ell = 0.005$ are made of rock-like materials which have $c_V = 800$ J/(kg K) and $\rho = 2600$ kg/m^3 as specific heat (at constant volume) and material density. The relaxation time τ and the heat parameter κ^2 as new material constants have been measured earlier for several realistic cases in [1]. On the basis of these experimental data, we choose 0.01 s and 0.001 s for τ, as well as the quite small 0.000008 m^2 for κ^2.

Since from numerical point of view the accurate modeling the thermal process is much more challenging task for high κ^2-values than low ones, also, the mixed *hp*-FEM presented in the latter section will be tested for the much less realistic but quite high value $\kappa^2 = 0.8$ m^2. Namely, this material constant has significant effect on the characteristic speed of the diffusion process and the heat propagation becomes faster with five magnitudes for the previous parameter setting ($\kappa^2 = 0.8$ m^2).

During the convergence analyzes, the time-dependent matrix algebraic system (30), or (29) together with Eq. (28) will be numerically-solved on the short time intervals $t \in [0, 0.1]$ s and $t \in [0, 1]$ s ($t_0 = 0$ s and $t_1 = \{0.1, 1\}$ s), respectively, for $\kappa^2 = 0.8$ m^2 and $\kappa^2 = 0.000008$ m^2, because the relatively high κ^2-value makes the rapidly change, i.e., computationally interesting (transient) region much shorter. The temporal integration will be executed numerically, using the implicit scheme [23]. The time step size will be set to the constant $\Delta t = 0.001$ s, leading to the time step numbers 100 and 1000.

4.2. Exponentially changing heating process

In the first numerical example a heat flow with relatively high, exponentially changing rate is acted on the left-hand-sided boundary ($x = 0$) as temporal prescription

$$\tilde{q}_0(t) = \hat{q}\, \frac{c_1\, c_2}{c_2 - c_1} \left[\exp\left(-c_1 \frac{t}{t_p} \right) - \exp\left(-c_2 \frac{t}{t_p} \right) \right], \tag{34}$$

while a heat transfer BC is imposed at the right-hand-side ($x = \ell$) as

$$\tilde{q}_\ell(t) = h \left[T(t,\ell) - T_0(\ell) \right], \tag{35}$$

with which the ICs $T_0(x) = 293$ K and $q_0(x) = 0$ W/m^2 as applied spatial prescriptions at $t_0 = 0$ s are of course compatible, namely the body is initially at rest, i.e., in termodynamic equilibrium. In Eq. (34), the parameters are set to $\hat{q} = 10000$ W/m^2, as well as $c_1 = 1/0.075$, $c_2 = 6$ and $t_p = 0.008$ s according to the reference [2], in order to make the above-considered heat conductivity problem most realistic. Besides, the heat transfer coefficient appeared in the thermal convection BC (35) is selected from the discrete value set $\{0, 100, 1000, 10000\}$ W/(m^2 K). If we choose 0 W/(m^2 K) for the heat transfer coefficient h, the special form of the BC (35) is obtained, where the radiated heat flow to or from the ambient through the boundary $x = \ell$ is zero, i.e., this boundary becomes adiabatic insulation. In this example, the influence of the heat transfer coefficient on the quality, i.e., the solution and the convergence of the *h*- and *p*-version FE approximation is studied as well.

The reason, why this test example is selected, is that the classical *h*-version FEMs and commercial FE softwares provide unreliable and inaccurate or quite wrong numerical results, these products do not work satisfactorily because the related FEs do not treat appropriately the BCs and do not set correct function spaces to the variables, see, for example the bad numerical results provided by COMSOL in [20].

During the convergence studies, the *p*-extensions are performed on a 4- and 48-element fixed uniform mesh of the region Ω, respectively, for overdiffuse and non-overdiffuse thermodynamic systems, i.e., for the parameter values $\kappa^2 = 0.8$ m^2 and $\kappa^2 = 0.000008$ m^2 with the polynomial degree p ranging from 1 to 7, whereas the *h*-extensions are executed on equidistant meshes, varying the element number n in 7 steps from 4 and 48 to 16 and 120, respectively, for overdiffuse ($\kappa^2 = 0.8$ m^2) and non-overdiffuse ($\kappa^2 = 0.000008$ m^2) thermal processes. At all of the *h*-refinement steps the degree of the polynomial approximation $p = 1$ is kept unchanged on each element.

The relative- and absolute errors measured in the maximum norms (33) of the front- and rear-sided temperature $T(t,0)$ and $T(t,\ell)$, as well as the front- and rear-sided heat flow, $q(t,0)$ and $q(t,\ell)$, as time series calculated for quite high and very small κ^2-value (0.8 m^2 and 0.000008 m^2) are plotted versus number of DOF in double logarithmic scale for the relaxation times $\tau = 0.01$ s and $\tau = 0.001$ s in Figs. 2–5. Since both BCs (3)–(4) are built in the variational formulations (18)–(20) or (21)–(23). i.e., these are ensured in a weak sense, it is worth investigating the convergence behavior of not only the non-relaxed- but also the relaxed (or weakly-imposed) variables at both boundaries, thereby obtaining information also for how precisely the BCs are satisfied during the thermal conductivity process. If the heat transfer coefficient h be equal to 0 W/(m^2 K) at the right-hand-sided boundary during the numerical tests, the heat flow becomes 0 W/m^2. Therefore, only the absolute (not the relative) error of the heat flow and its convergences can be computed at this boundary ($x = \ell$).

The relative- and the absolute error series have monotonic convergence with relatively high rates not only for the *p*-approximation but also for the lowest-degree *h*-approximation ($p = 1$). The *h*-extensions show algebraic convergence behavior, i.e., the convergence rates are independent of the DOF. The *h*-convergence is faster with about one magnitude for the heat flow than for the temperature. The explanation for this numerical result is that the heat flow has to be approximated by a polynomial of a higher degree than the temperature, see again Table 1. The *p*-extensions exhibit exponential convergences with increasing negative slopes in the asymptotic region. As expected, the *p*-convergence is much faster than the *h*-convergence. It can be observed that the achievable relative error level is almost equal or less than about 10^{-8}. Consequently high numerical accuracy can be reached.

Also, it can be experienced that there is no significant effect of the heat transfer coefficient h on either the *h*- and *p*-convergence rates, the

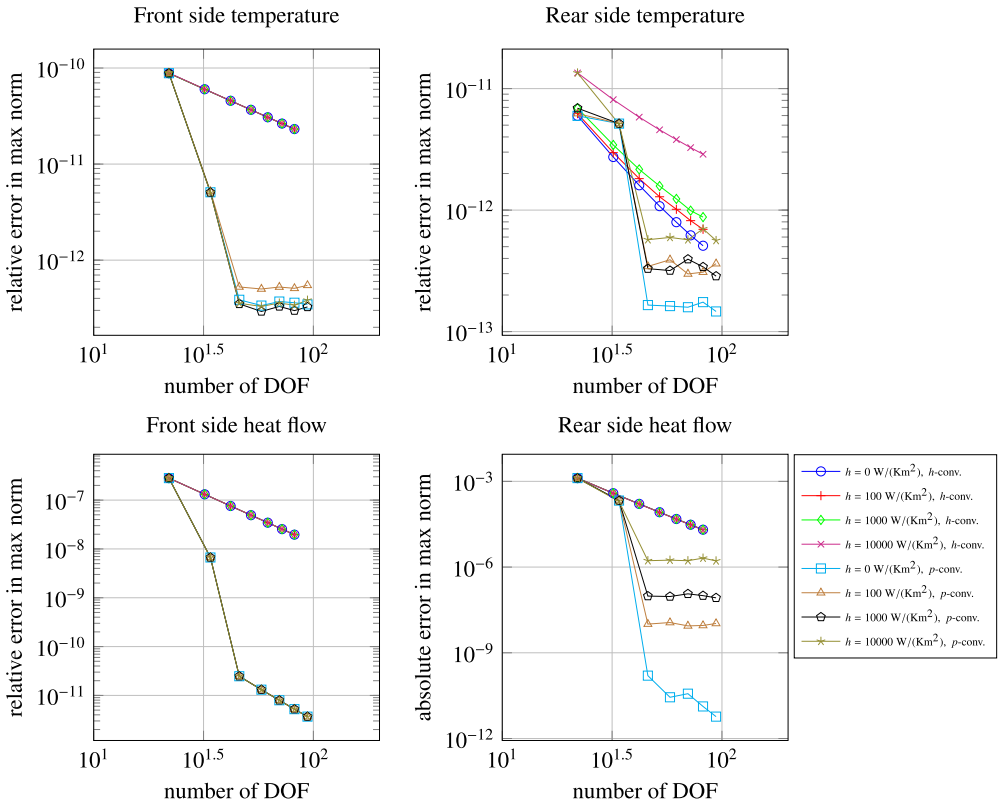

Fig. 2. Convergence curves of the errors measured in max. norm for the front- and rear side temperature and heat flow: overdiffuse system with $\tau = 0.001$ s and $\kappa^2 = 0.8$ m^2.

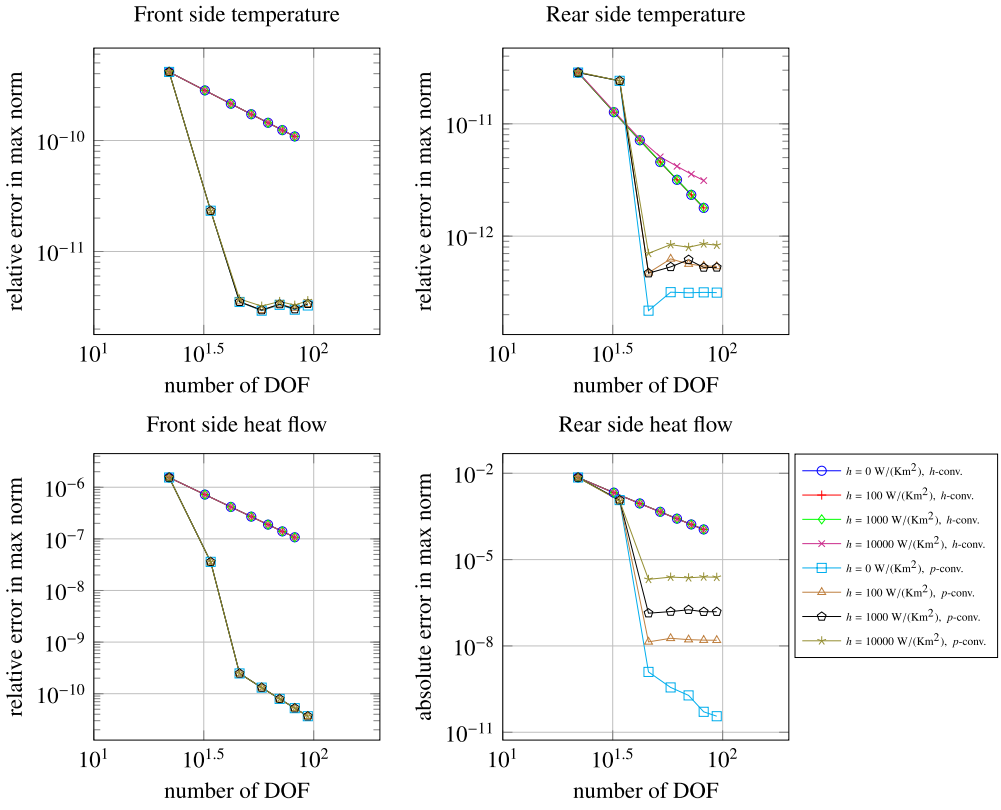

Fig. 3. Convergence curves of the errors measured in max. norm for the front- and rear side temperature and heat flow: overdiffuse system with $\tau = 0.01$ s and $\kappa^2 = 0.8$ m^2.

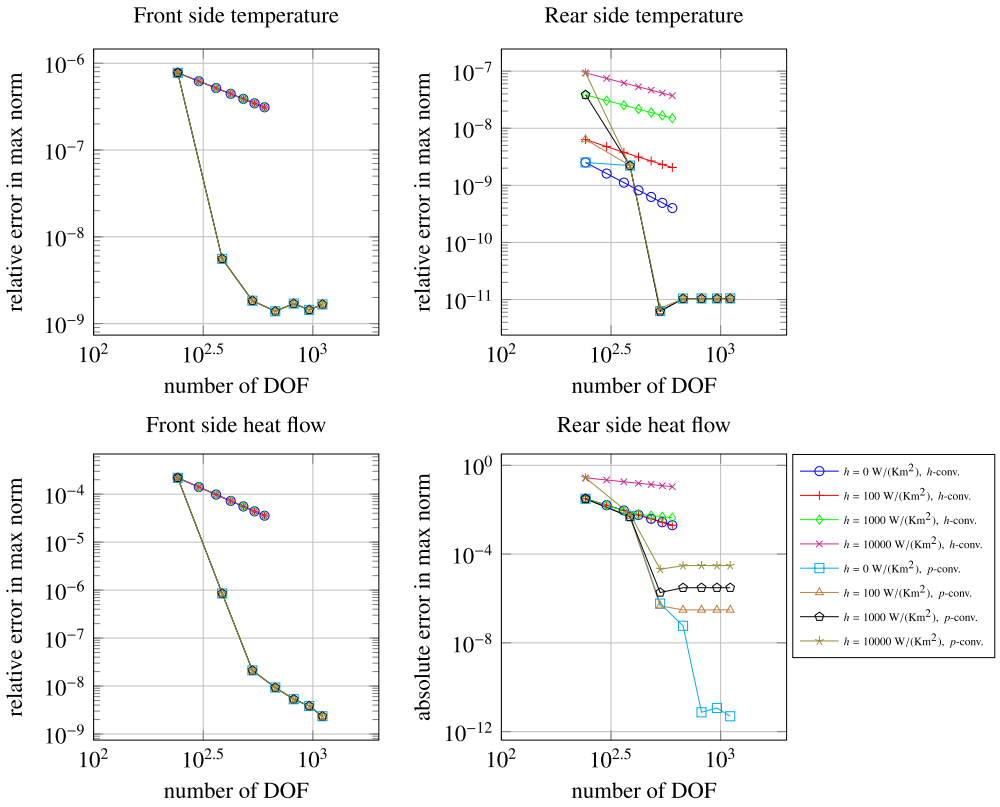

Fig. 4. Convergence curves of the errors measured in max. norm for the front- and rear side temperature and heat flow: non-overdiffuse exponentially changing heating system with $\tau = 0.001$ s and $\kappa^2 = 0.000008$ m^2.

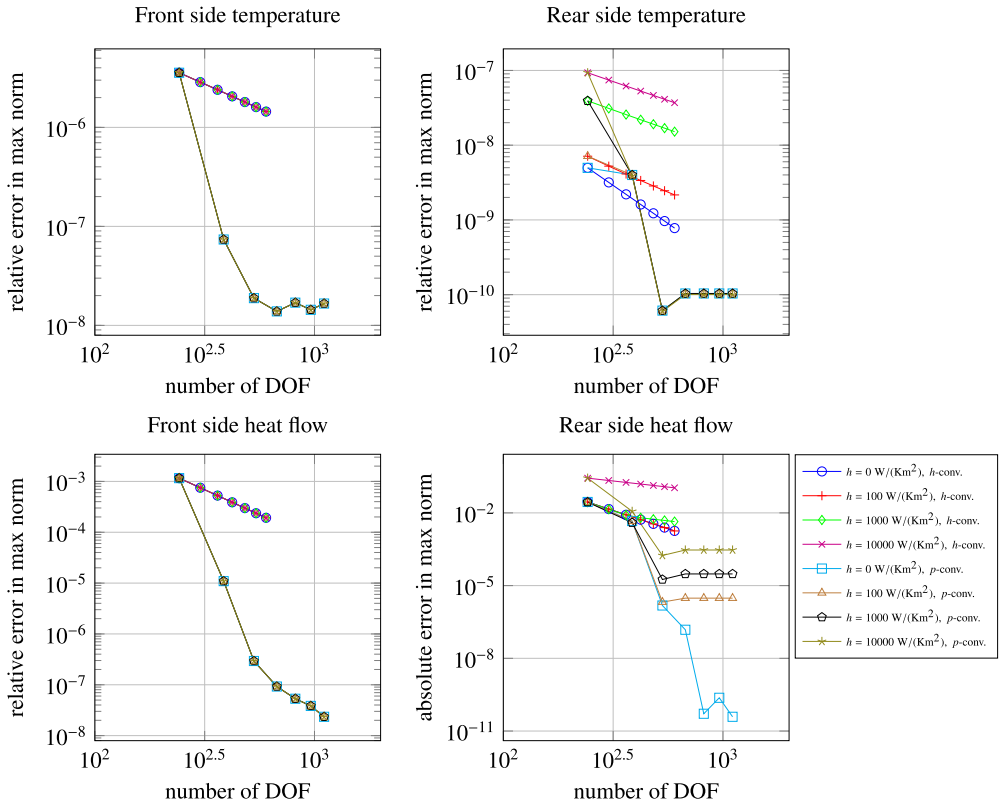

Fig. 5. Convergence curves of the errors measured in max. norm for the front- and rear side temperature and heat flow: non-overdiffuse exponentially changing heating system with $\tau = 0.01$ s and $\kappa^2 = 0.000008$ m^2.

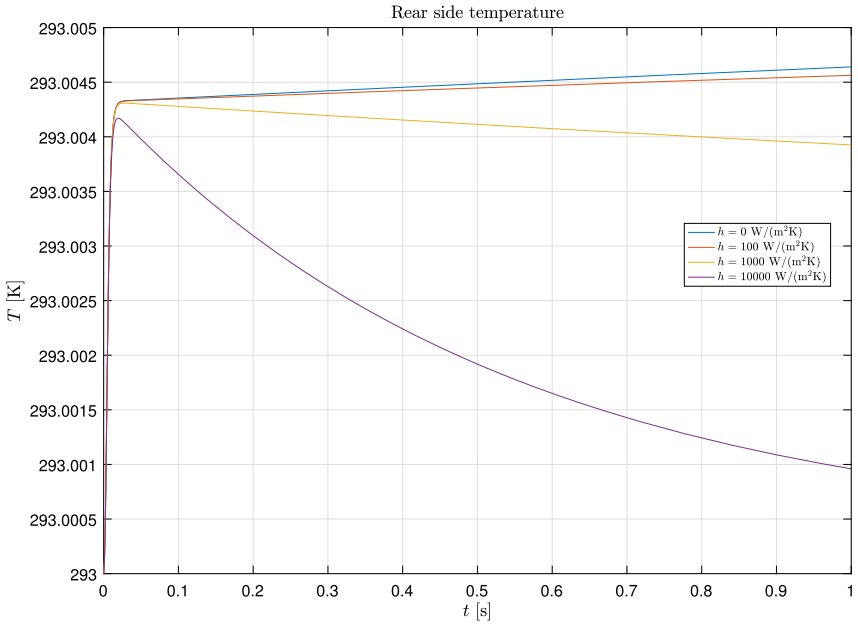

Fig. 6. Short time history of the rear side temperature for non-overdiffuse exponentially changing heating system with $\tau = 0.01$ s.

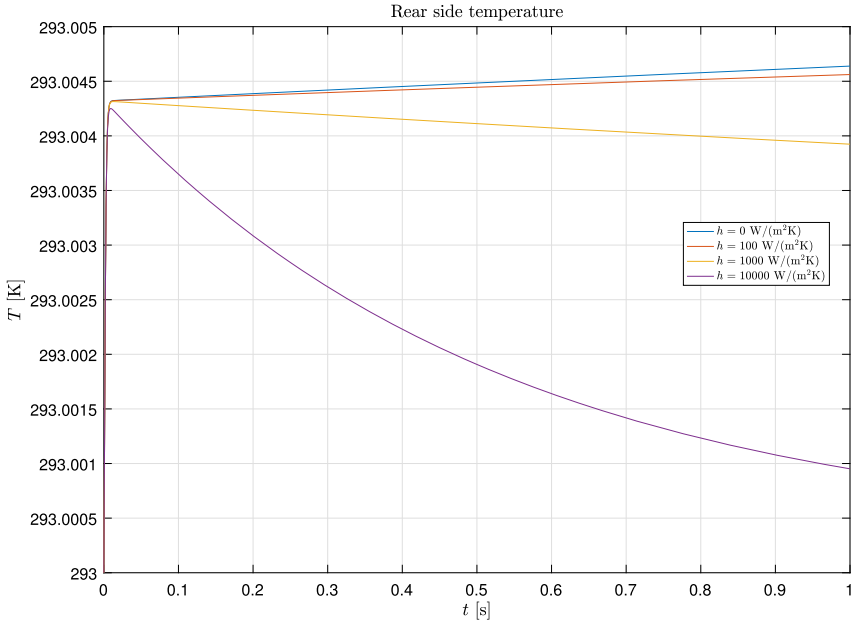

Fig. 7. Short time history of the rear side temperature for non-overdiffuse exponentially changing heating system with $\tau = 0.001$ s.

convergence curves at the rear-sided boundary are shifted down a bit without changing their slopes as the heat transfer coefficient h is reduced from the value 10000 W/(m^2 K) to 0 W/(m^2 K) thereby achieving bit lower error levels. But there is no remarkable difference between these error levels.

Let us illustrate now the hp-FE solutions of the model problem. In order to make good impression of the accuracy and effectivity (exemption from oscillation) of the developed mixed hp-FEM, this test problem is solved for the time interval $t \in [0, 1]$ s and a longer one $t \in [0, 10]$ by applying a 100-element mesh together with the high polynomial degree $p = 10$, thereby keeping the time step size $\Delta t = 0.001$ fixed. The time series obtained for the rear sided temperature responses are plotted for non-overdiffuse system in Figs. 6–9 and for overdiffuse thermal process in Figs. 10–13 in the case of $\tau = 0.01$ s and $\tau = 0.001$ s, representing the influence of the heat transfer coefficient on the numerical solutions.

It can be seen that oscillations can not be experienced at all even for the long term solutions. After the initial rapid temperature increment, the cooling process becomes faster as the heat transfer coefficient h increases. Besides, the thermal equilibrium state can be reached earlier for overdiffuse heat conductivity processes than for non-overdiffuse ones.

4.3. Ramp-type heating process

In the second numerical example a ramp-type surface heating process is modelled. In this framework, a temperature BC is specified at the left-hand-side $x = 0$ as temporal jump function

$$\tilde{T}(t) = \begin{cases} \hat{T}\,\dfrac{t}{t_p} & \text{for} \quad t \in [0, t_p]\,, \\ \hat{T} & \text{for} \quad t \in (t_p, \infty]\,, \end{cases} \tag{36}$$

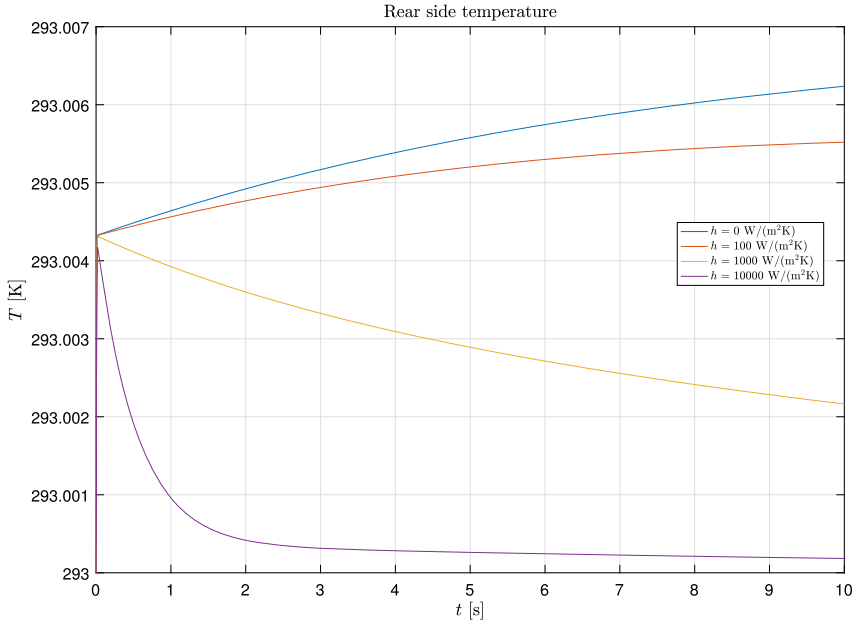

Fig. 8. Long time history of the rear side temperature for non-overdiffuse exponentially changing heating system with $\tau = 0.01$ s.

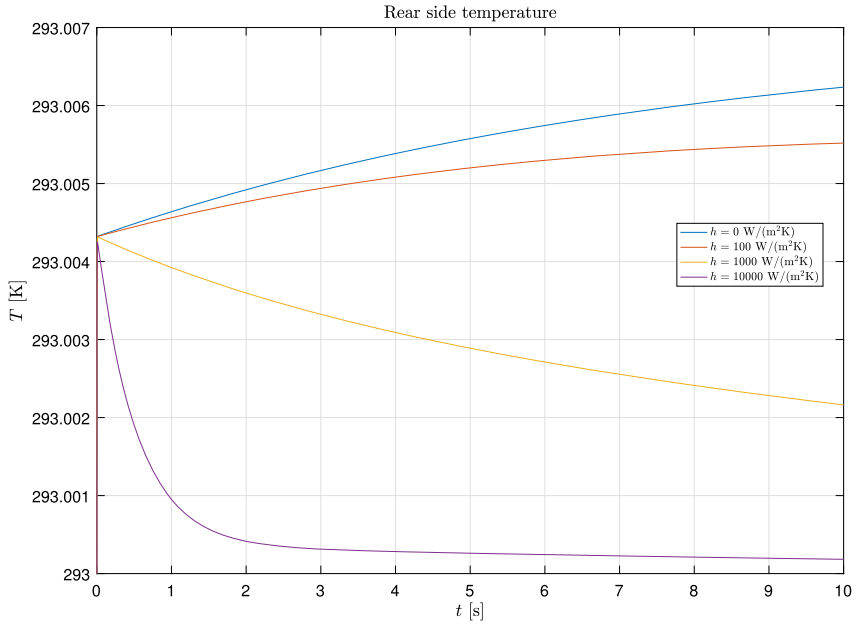

Fig. 9. Long time history of the rear side temperature for non-overdiffuse exponentially changing heating system with $\tau = 0.001$ s.

in which $\hat{T} = 398$ K is the temperature maximum and $t_p = 0.008$ s is the temporal length of the ramp phase, whereas the right-hand-sided boundary keeps insulated adiabatically, i.e., the constant, homogeneous BC $\tilde{q}_\ell(t) = 0$ W/m^2 is prescribed in time at $x = \ell$ for the heat flow. Besides, the body is exposed to the spatial impositions $T_0(x) = 293$ K and $q_0(x) = 0$ W/m^2 as ICs on the temperature and the heat flow that are consistent with the BCs at $t_0 = 0$ s. Accordingly, again the body is initially at rest, i.e., in equilibrium state.

For these types of benchmark problems, numerical oscillations can appear in the time history of either the temperature or the heat flow. In this specific test problem the exact solution produces discontinuities (jumps) at certain time instants especially in the time series of the heat flow. Near these certain jumps the oscillatory behavior of the FE solution is observed around the analytic solution when using the classical, lower-order, h-version FEMs for the solution of the IBVP in question, see the background and some numerical results, for example, in [33]. This is the main reason why this benchmark problem is chosen now as second test example.

During the convergence analyzes the p-extensions are implemented on a 12- and 48-element fixed equidistant mesh, respectively, for non-overdiffuse ($\kappa^2 = 0.000008$ m^2) and overdiffuse ($\kappa^2 = 0.8$ m^2) thermal processes with p being uniformly increased from 2 to 11, while the h-extensions were carried out on uniformly refined meshes with the element number n ranging in 14 steps from 12 and 48 to 90 and 204, respectively, for non-overdiffuse and overdiffuse thermodynamic systems, i.e., for $\kappa^2 = 0.000008$ m^2 and $\kappa^2 = 0.8$ m^2.

Once again, the error values are computed on the basis of the maximum norms defined in Eq. (33). Then the relative error convergence curves of the temperatures $T(t,0)$ and $T(t,\ell)$, as well as the front-sided heat flow $q(t,0)$ and the absolute error convergences of the rear-sided heat flow $q(t,\ell)$ are plotted against the number of DOF on log-log scales in Figs. 14–15 for the small and large κ^2-value (0.000008 m^2 and 0.8 m^2).

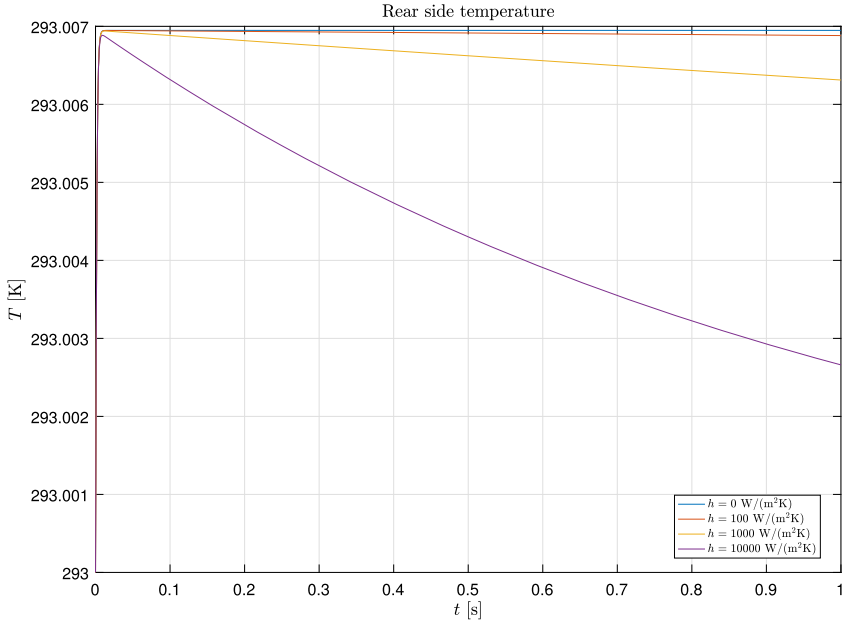

Fig. 10. Short time history of the rear side temperature for overdiffuse exponentially changing heating system with $\tau = 0.01$ s.

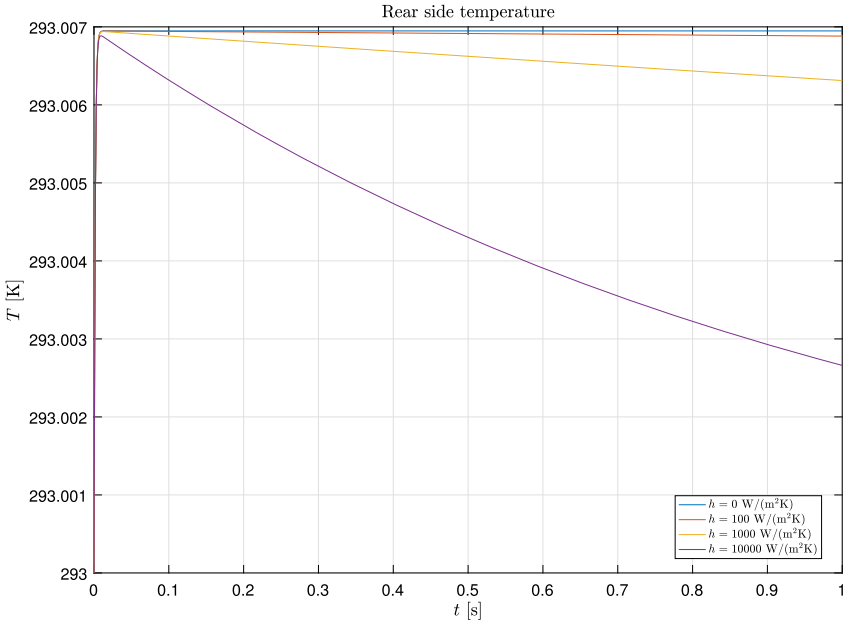

Fig. 11. Short time history of the rear side temperature for overdiffuse exponentially changing heating system with $\tau = 0.001$ s.

Here, the effect of the relaxation time τ on the convergence histories is also observed a bit.

Again, the relative and absolute error convergences show locking-free behaviors, i.e., no oscillations can be experienced at either the p- or the h-extensions. The h-extensions have algebraic convergences, i.e., their rates do not depend on the number of DOF. There is no significant influence of the relaxation time τ on the convergence rates. However, mainly the h-convergence curves are shifted down with approximately one magnitude without varying their slopes as the relaxation time decreases, i.e., changing it from $\tau = 0.01$ s to $\tau = 0.001$ s.

The p-extension shows exponentially increasing convergence rates in the asymptotic range. As expected again, the rate of p-convergences is much higher than that of h-convergences. It can be seen that the reachable error levels are equal to or rather less than about 10^{-5} for non-overdiffuse thermal processes. In the post-asymptotic range the exponential p-convergences slow down a bit for overdiffuse systems, then their rates are increasing again with negative slopes, thereby approaching quite small relative and absolute error levels (approximately 10^{-5} and 10^{-8}), i.e., also in this benchmark problem, quite high accuracy can be achieved. Besides, it is important to mention here that the convergences of the front-sided temperature and the rear-sided heat flow represent how accurately the satisfaction of the BCs is numerically ensured in weak form. Accordingly, these are enforced with great precision.

Once again, in order to make good impression of the reliability and efficiency of the constructed mixed hp-FEM on the reader, the ramp-type heating problem is solved for the quite short temporal domain $t \in [0, 0.1]$ by using a 100-element, equidistant mesh along with a very high polynomial approximation $p = 10$ on each element and setting the time step size to the constant value $\Delta t = 0.001$ s. Since this thermal process is

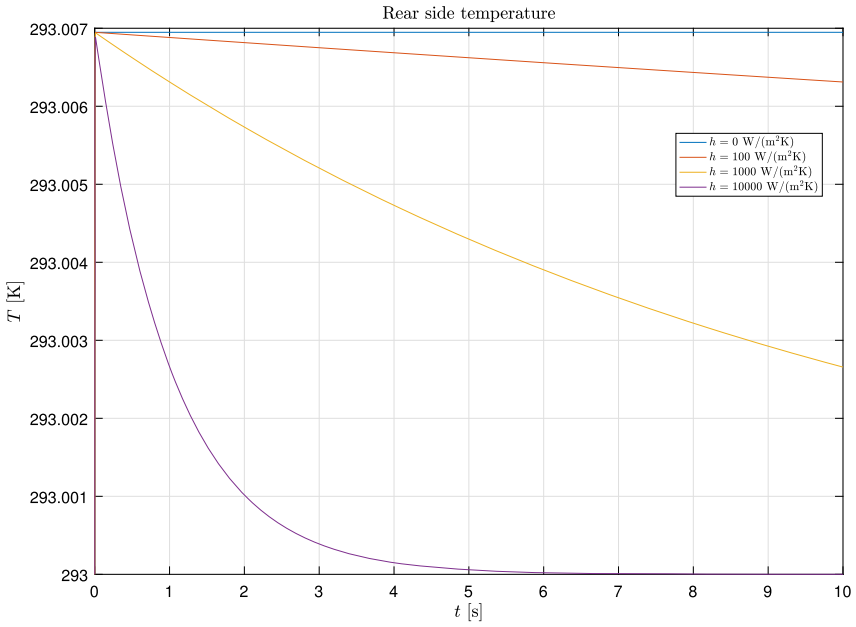

Fig. 12. Long time history of the rear side temperature for overdiffuse exponentially changing heating system with $\tau = 0.01$ s.

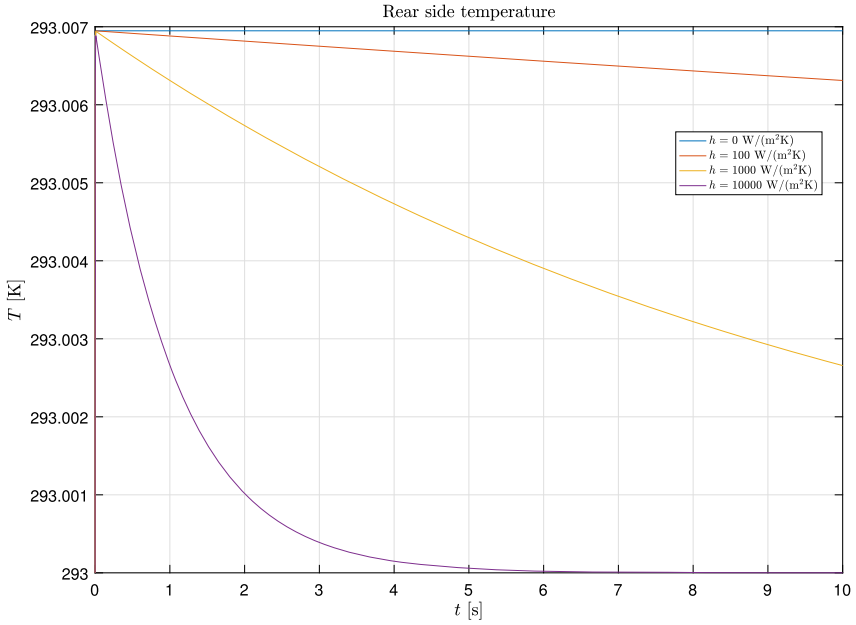

Fig. 13. Long time history of the rear side temperature for overdiffuse exponentially changing heating system with $\tau = 0.001$ s.

very fast, it is not needed to solve numerically this IBVP on a longer time interval, the nice characteristics of the solution will be well apparent in this temporal domain as well. The time histories obtained for the front-sided heat flow and the rear-sided temperature as non-prescribed response functions are depicted, respectively, for non-overdiffuse and overdiffuse thermodynamic systems in Figs. 16–17 and 18–19 in the case of $\tau = 0.01$ s and $\tau = 0.001$ s, thereby, also, indicating the influence of the relaxation time on the numerical solution.

It can be seen that oscillation-free, i.e., locking-free numerical behavior can be experienced at a very large number of DOF as well. The *hp*-FE solutions are accurate and stable. During these ramp-type heating processes at the very beginning the temperature is rapidly increasing, then achieving a constant equilibrium temperature. This initial rapid temperature increment is linear function of time for overdiffuse systems, see Fig. 19, whereas this is a smoothly varying function with rapidly increasing then rapidly decreasing positive slope for non-overdiffuse thermal conductivity problems, see Fig. 17.

For overdiffuse thermodynamic systems a rectangular shaped heat flow train is obtained as response function at the rear side $x = \ell$ due to the ramp-type temperature increment at the front side $x = 0$, see Fig. 18, while for non-overdiffuse thermal processes the heat flow train at the rear-sided boundary $x = \ell$ consists of an increasing- and a decreasing part which change smoothly with decreasing positive, then decreasing negative slopes, see Fig. 16.

5. Concluding remarks and future perspectives

A new mixed *hp*-FEM was developed for the solution of the Guyer–Krumhansl heat conductivity model as one of the IBVPs in the refined thermodynamics. The constructed FEM is based on a new three-field

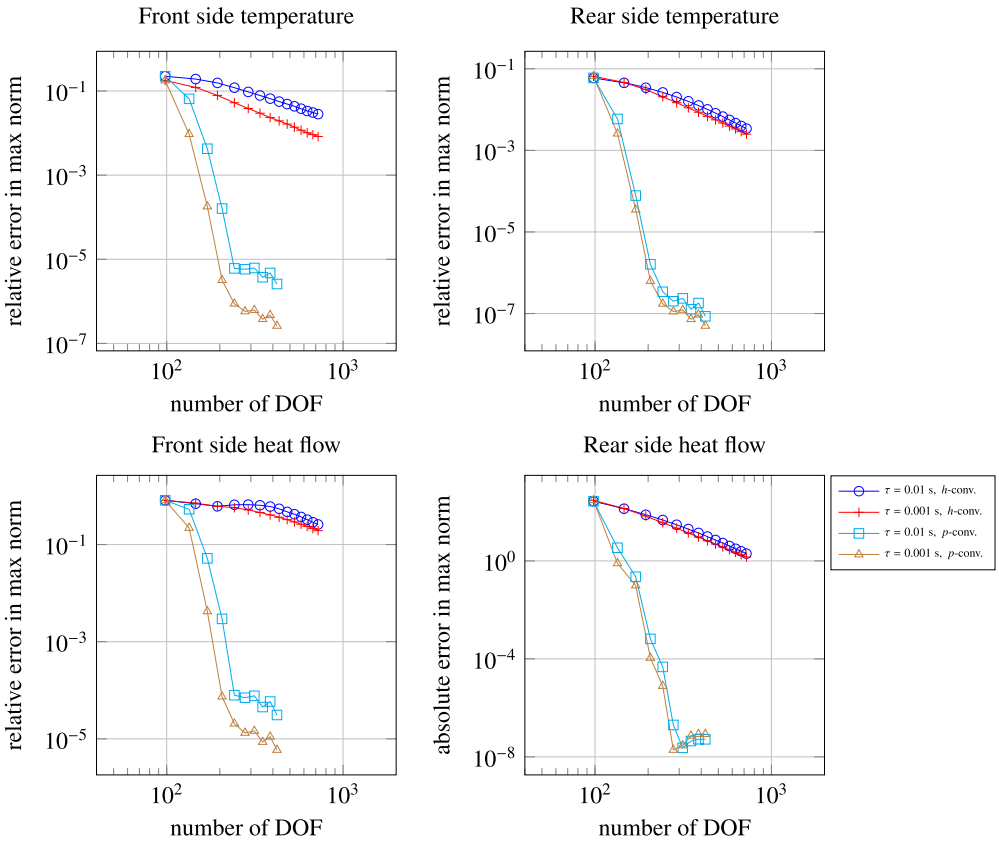

Fig. 14. Convergence curves of the errors measured in max. norm for the front- and rear side temperature and heat flow: non-overdiffuse, ramp-type heating system with $\tau = 0.01$ s, $\tau = 0.001$ s and $\kappa^2 = 0.000008$ m^2.

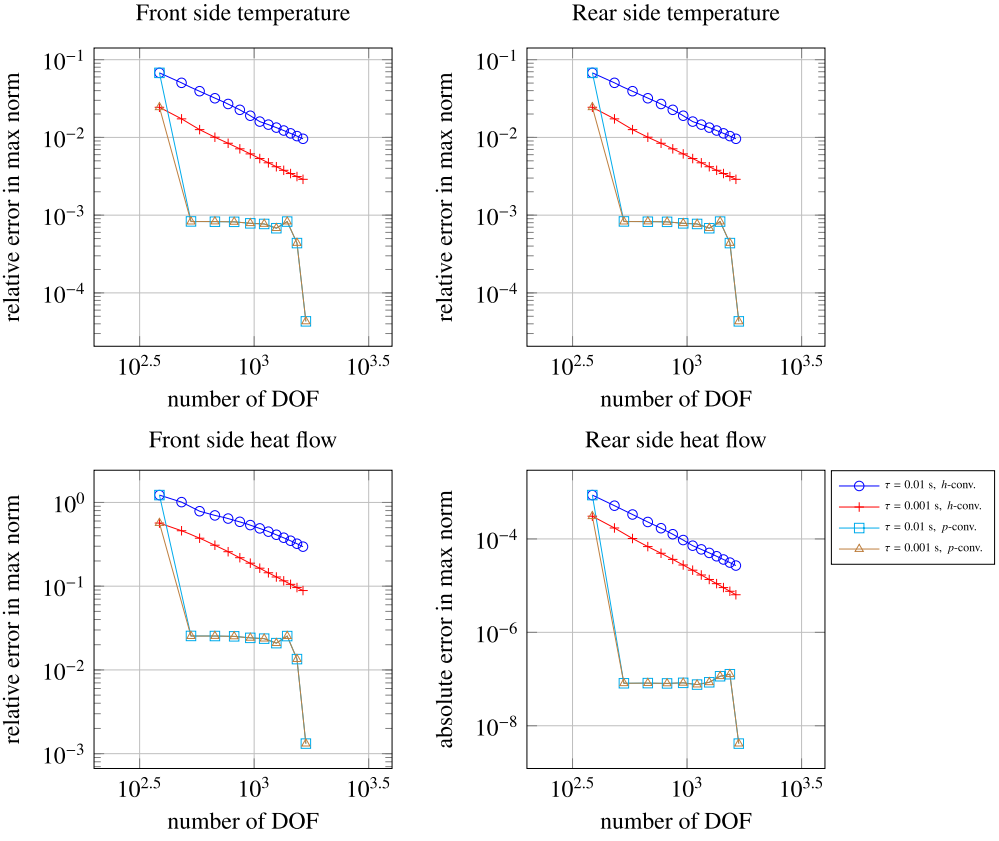

Fig. 15. Convergence curves of the errors measured in max. norm for the front- and rear side temperature and heat flow: overdiffuse, ramp-type heating system with $\tau = 0.01$ s, $\tau = 0.001$ s and $\kappa^2 = 0.8$ m^2.

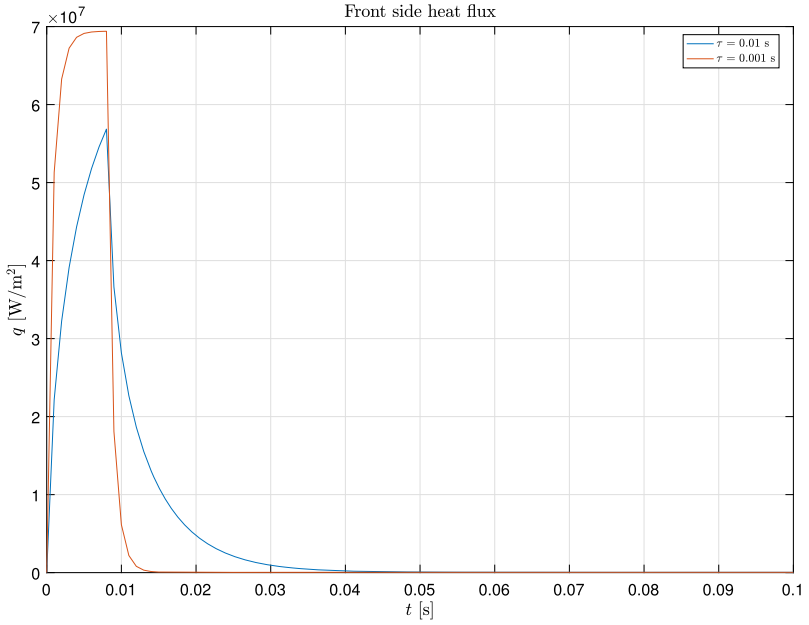

Fig. 16. Time history of the front side heat flow for non-overdiffuse ramp-type heating process with $\tau = 0.01$ s and $\tau = 0.001$ s.

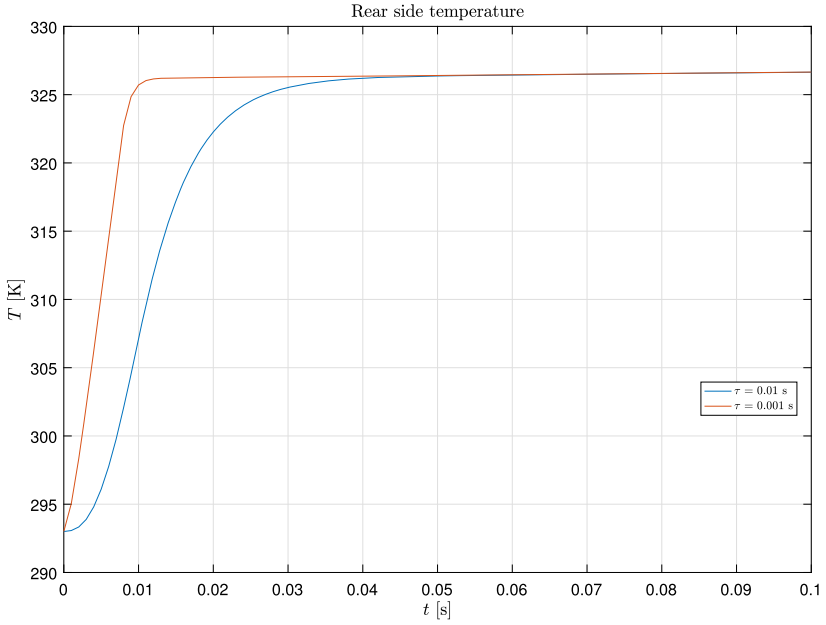

Fig. 17. Time history of the rear side temperature for non-overdiffuse ramp-type heating process with $\tau = 0.01$ s and $\tau = 0.001$ s.

variational formulation allowing the temperature, the heat flow and the current density of the heat flow to be independently varied. The current density of the heat flow, i.e., its global vector containing unknown coefficients has been eliminated at element level. This procedure, similarly to the Schur complement technique, has yielded a time dependent linear algebraic equation system for the temperature and heat flow vectors consisting of the unknown coefficients. The resulting system of equation has been solved for the coefficients at each time instant, using the unconditionally stable implicit time integration scheme.

Firstly, the numerical predict capability of the *hp*-FEM was tested through *h*- and *p*-convergence analyzes for an exponentially changing, rapid heating process. The relative and absolute errors were determined in maximum norm. It was proven computationally for both non-overdiffuse and overdiffuse thermodynamic processes that the convergences are fast. Robust (uniformly stable) convergence results have been obtained. However, the rate of the *p*-convergence is much higher than that of *h*-convergence, i.e., the desired (high) accuracy is achieved much earlier with *p*-extension than with *h*-refinement.

Secondly, similarly to the previous benchmark problem, oscillation-free, or, in other words, locking-free behavior of the newly-constructed *hp*-FEM was numerically experienced not only at *h*- but also at *p*-extension for the ramp-type, sudden heating process as well. To summarize, the mixed *hp*-version FEM is reliable and efficient, providing convergent and accurate results for the response functions of both the temperature and the heat flow in the case of either relatively high or very small κ^2-values. Aware of the outstanding computational results the three-field mixed *hp*-FEM demonstrated in this paper will be further-developed for the solution of (i) non-smooth- (singular-) and/or (ii) 2- and 3D IBVPs related to (iii) heterogeneous materials, which will be already tested on the new analytic solution derived for the 2D axisymmetric IBVP of the Guyer–Krumhansl model in [47].

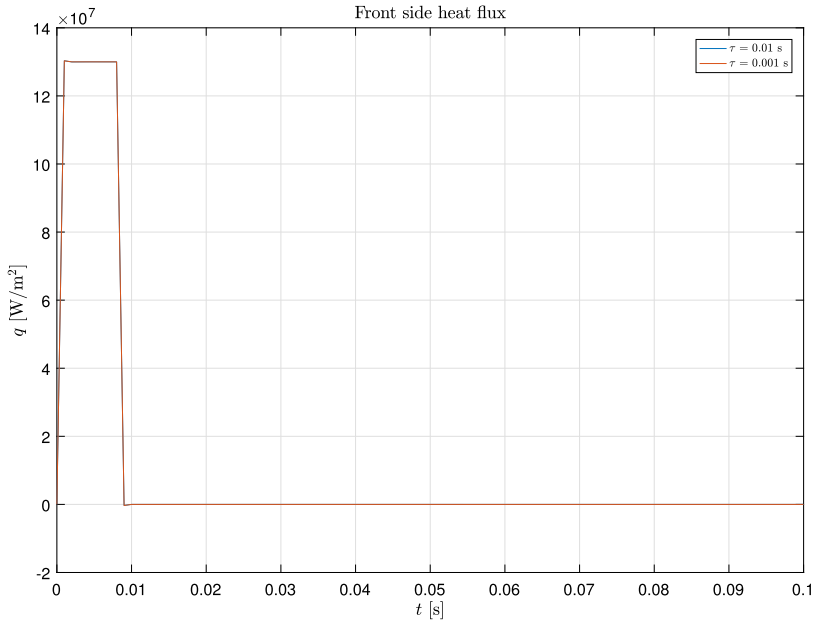

Fig. 18. Time history of the front side heat flow for overdiffuse ramp-type heating process with $\tau = 0.01$ s and $\tau = 0.001$ s.

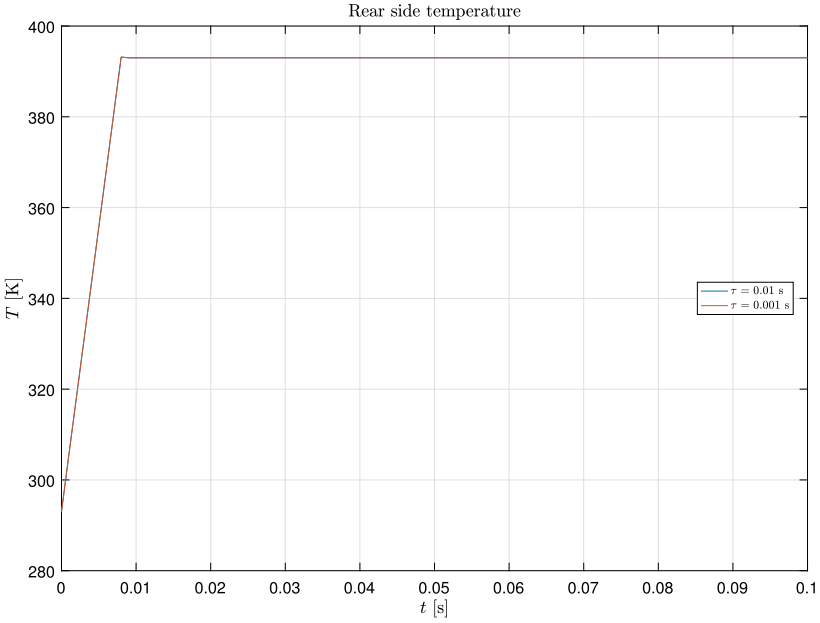

Fig. 19. Time history of the rear side temperature for overdiffuse ramp-type heating process with $\tau = 0.01$ s and $\tau = 0.001$ s.

CRediT authorship contribution statement

The author Balázs Tóth is responsible for the conceptualization, the methodology, the software, the validation, the visualization and writing – original draft, review & editing.

Declaration of competing interest

Balazs Toth reports financial support was provided by National Research Development and Innovation Office. Balazs Toth reports a relationship with National Research Development and Innovation Office that includes.

Data availability

No data was used for the research described in the article.

Acknowledgements

The research work reported in this paper has been supported by the National Research, Development and Innovation Office-NKFIH under grant No. FK 134277.

References

[1] S. Both, B. Czél, T. Fülöp, G. Gróf, Á. Gyenis, R. Kovács, P. Ván, J. Verhás, Deviation from the Fourier law in room-temperature heat pulse experiments, J. Non-Equilib. Thermodyn. 41 (2016) 41–48.

[2] A. Fehér, R. Kovács, On the evaluation of non-Fourier effects in heat pulse experiments, Int. J. Eng. Sci. 169 (2021) 103577, arXiv:2101.01123.

[3] A. Lunev, A. Lauerer, V. Zborovskii, F. Léonard, Digital twin of a laser flash experiment helps to assess the thermal performance of metal foams, Int. J. Therm. Sci. 181 (2022) 107743.

[4] S. Sobolev, I. Kudinov, Heat conduction across 1D nano film: local thermal conductivity and extrapolation length, Int. J. Therm. Sci. 159 (2021) 106632.
[5] R.A. Guyer, J.A. Krumhansl, Thermal conductivity, second sound, and phonon hydrodynamic phenomena in nonmetallic crystals, Phys. Rev. 148 (1966) 778–788.
[6] R. Kovács, A. Fehér, S. Sobolev, On the two-temperature description of heterogeneous materials, Int. J. Heat Mass Transf. 194 (2022) 123021.
[7] S. Sobolev, Heat conduction equation for systems with an inhomogeneous internal structure, J. Eng. Phys. Thermophys. 66 (1994) 436–440.
[8] S.L. Sobolev, Local non-equilibrium transport models, Phys. Usp. 40 (1997) 1043.
[9] A. Vedavarz, S. Kumar, M. Moallemi, Significance on non-Fourier heat waves in microscale conduction, in: Micromechanical Sensors, Actuators, and Systems, American Society of Mechanical Engineers, Dynamic Systems and Control Division (Publication) DSC, ASME, 1991, pp. 109–122, Winter Annual Meeting of the American Society of Mechanical Engineers.
[10] A. Vedavarz, S. Kumar, M. Moallemi, Significance of non-Fourier heat waves in conduction, J. Heat Transf. 116 (1994) 221–224.
[11] W. Kaminski, Hyperbolic heat conduction equation for materials with a nonhomogeneous inner structure, J. Heat Transf. 112 (1990) 555–560.
[12] K. Mitra, S. Kumar, A. Vedevarz, M.K. Moallemi, Experimental evidence of hyperbolic heat conduction in processed meat, J. Heat Transf. 117 (1995) 568–573.
[13] I. Müller, T. Ruggeri, Rational Extended Thermodynamics, Springer-Verlag, New York, 1998.
[14] P. Ván, T. Fülöp, Universality in heat conduction theory – weakly nonlocal thermodynamics, Ann. Phys. (Berlin) 524 (2012) 470–478.
[15] R. Kovács, Analytic solution of Guyer–Krumhansl equation for laser flash experiments, Int. J. Heat Mass Transf. 127 (2018) 631–636.
[16] R. Kovács, Analytical treatment of nonhomogeneous initial states for non-Fourier heat equations, Int. Commun. Heat Mass Transf. 134 (2022) 106021.
[17] A. Ramos, L. Miranda, M. Freitas, R. Kovács, Non-negativity and maximum principle: revisiting the Guyer–Krumhansl heat equation, Int. J. Heat Mass Transf. 211 (2023) 124288.
[18] K. Zhukovsky, Exact solution of Guyer–Krumhansl type heat equation by operational method, Int. J. Heat Mass Transf. 96 (2016) 132–144.
[19] K. Zhukovsky, D. Oskolkov, Modeling of heat transport and exact analytical solutions in thin films with account for constant non-relativistic motion, Int. J. Heat Mass Transf. 150 (2020) 119085.
[20] A. Rieth, R. Kovács, T. Fülöp, Implicit numerical schemes for generalized heat conduction equations, Int. J. Heat Mass Transf. 126 (2018) 1177–1182.
[21] A. Ramos, R. Kovács, M. Freitas, D. Almeida Júnior, Mathematical analysis and numerical simulation of the Guyer–Krumhansl heat equation, Appl. Math. Model. 115 (2023) 191–202.
[22] K.-J. Bathe, Finite Element Procedures, Prentice Hall, Upper Saddle River, New Jersey, 1996.
[23] T.J.R. Hughes, The Finite Element Method: Linear Static and Dynamic Finite Element Analysis, Prentice Hall, Englewood Cliffs, New Jersey, 1987.
[24] J.N. Reddy, Energy Principles and Variational Methods in Applied Mechanics, 2nd ed., John Wiley & Sons, New York, 2002.
[25] B. Deka, J. Dutta, Finite element methods for non-Fourier thermal wave model of bio heat transfer with an interface, J. Appl. Math. Comput. 62 (2020) 701–724.
[26] B. Deka, J. Dutta, Convergence of finite element methods for hyperbolic heat conduction model with an interface, Comput. Math. Appl. 79 (2020) 3139–3159.
[27] H. Gómez, I. Colominas, F. Navarrina, M. Casteleiro, A finite element formulation for a convection–diffusion equation based on Cattaneo's law, Comput. Methods Appl. Mech. Eng. 196 (2007) 1757–1766.
[28] A. van der Merwe, N. van Rensburg, R. Sieberhagen, Comparing the dual phase lag, Cattaneo-Vernotte and Fourier heat conduction models using modal analysis, Appl. Math. Comput. 396 (2021) 125934.
[29] H. Nazmdeh, M. Vahabi, M.A. Nazari, Finite element modeling of non-Fourier heat transfer in a cancerous tissue with an injected fat layer during hyperthermia treatment, J. Therm. Biol. 100 (2021) 103073.
[30] B. Xu, B.Q. Li, Finite element solution of non-Fourier thermal wave problems, Numer. Heat Transf., Part B, Fundam. 44 (2003) 45–60.
[31] Z.-B. Yang, Z.-K. Wang, S.-H. Tian, X.-F. Chen, Analysis and modelling of non-Fourier heat behavior using the wavelet finite element method, Materials 12 (2019).
[32] G. Capriz, K. Wilmanski, P.M. Mariano, Exact and approximate Maxwell–Cattaneo-type descriptions of heat conduction: a comparative analysis, Int. J. Heat Mass Transf. 175 (2021) 121362.
[33] G. Apostolakis, G.F. Dargush, Variational methods in irreversible thermoelasticity: theoretical developments and minimum principles for the discrete form, Acta Mech. 224 (2013) 2065–2088.
[34] B. Szabó, I. Babuška, I.N. Katz, The p-version of the finite element method, SIAM J. Numer. Anal. 18 (1981) 515–545.
[35] B. Szabó, I. Babuška, Introduction to Finite Element Analysis: Formulation, Verification and Validation, John Wiley & Sons, New York, 2011.
[36] B. Tóth, L.G. Kocsán, Comparison of dual-mixed h- and p-version finite element models for axisymmetric problems of cylindrical shells, Finite Elem. Anal. Des. 65 (2013) 50–62.
[37] B. Tóth, Hybridized dual-mixed hp-finite element model for shells of revolution, Comput. Struct. 218 (2019) 123–151.
[38] B. Tóth, D. Burmeister, Dual-mixed hp-version axisymmetric shell finite element using NURBS mid-surface interpolation, Acta Mech. 231 (2020) 2457–2483.
[39] B. Tóth, Natural frequency analysis of shells of revolution based on hybrid dual-mixed hp-finite element formulation, Appl. Math. Model. 98 (2021) 722–746.
[40] N.V. Roberts, S. Henneking, Time-stepping DPG formulations for the heat equation, Comput. Math. Appl. 95 (2021) 242–255, Recent Advances in Least-Squares and Discontinuous Petrov–Galerkin Finite Element Methods.
[41] L. Demkowicz, Computing with hp-Adaptive Finite Elements: One- and Two-Dimensional Elliptic and Maxwell Problems, Applied Mathematics and Nonlinear Science, vol. I, Chapman & Hall/CRC Press, Taylor & Francis Group, 2007.
[42] A. Düster, E. Rank, B. Szabó, The p-version of the finite element and finite cell methods, in: Encyclopedia of Computational Mechanics, 2nd ed., John Wiley & Sons, Ltd, 2017, pp. 1–35.
[43] B. Tóth, Multi-field dual-mixed variational principles using non-symmetric stress field in linear elastodynamics, J. Elast. 122 (2016) 113–130.
[44] B. Tóth, Dual and mixed nonsymmetric stress-based variational formulations for coupled thermoelastodynamics with second sound effect, Contin. Mech. Thermodyn. 30 (2018) 319–345.
[45] S.C. Brenner, L.R. Scott, The Mathematical Theory of Finite Element Methods, 3rd ed., Springer-Verlag, New York, 2008.
[46] E. Sternberg, J.G. Chakravorty, On inertia effects in a transient thermoelastic problem, J. Appl. Mech. 26 (1959) 503–509.
[47] R. Kovács, Transient non-Fourier behavior of large surface bodies, arXiv:2306.17621, 2023.